Computer simulations of three-dimensional Turing patterns in the Lengyel-Epstein model

Hiroto Shoji[1] and Takao Ohta[2,3]

[1]*Department of Physics, Graduate School of Medical Science, Kyoto Prefectural University of Medicine, Taishogun, Kita-ku, Kyoto 603-8334, Japan*

[2]*Department of Physics, The University of Tokyo, Tokyo 113-0033, Japan*

[3]*Toyota Physical and Chemical Research Institute, Nagakute, Aichi 480-1192, Japan*

(Received 7 January 2015; published 19 March 2015)

We investigate numerically Turing patterns in the Lengyel-Epstein model in three dimensions. In a bulk homogeneous system under periodic boundary conditions, we obtain not only lamellar, cylindrical, and spherical structures but also several interconnected periodic structures including the Schwartz P-surface structure. In order to examine Turing patterns in the conditions accessible experimentally, we consider inhomogeneous systems where a parameter in the reaction-diffusion equations depends on the space coordinate with either Dirichlet or Neumann boundary conditions. In this situation, we find that a perforated-lamellar structure and an $Fddd$ structure, both of which have a uniaxial symmetry, appear depending on the boundary conditions.

DOI: 10.1103/PhysRevE.91.032913 PACS number(s): 89.75.Kd, 82.40.Ck, 47.54.Bd, 87.18.Hf

I. INTRODUCTION

In 1952 Turing showed mathematically that a two-component reaction-diffusion system with diffusion and nonlinear reaction terms exhibits spontaneous formation of spatially periodic structures if certain conditions are satisfied [1]. Experimental realization of Turing patterns was carried out by De Kepper and his coworkers [2,3] when they studied the chlorite-iodide-malonic acid (CIMA) reaction by open spatial reactors. Ouyang and Swinney achieved observing two-dimensional Turing patterns and their bifurcations of CIMA reaction in open thin gel reactors [4,5].

There are a number of theoretical studies of Turing patterns in two dimensions. See, for example, Ref. [6]. Typical patterns are stripe patterns and hexagonal disk-shaped patterns as experimentally observed [4]. In three dimensions, it is expected that there are many more varieties of Turing patterns since interconnected periodic structures are possible, which are characteristic of three dimensions. Earlier theoretical studies assuming homogeneity of the system [7–9] obtained numerically lamellar, cylindrical, and spherical domain patterns but could not make any definite conclusions about formation of interconnected structures.

In our previous papers [10,11], we investigated Turing structures in homogeneous three-dimensional (3D) systems by numerical simulations of the FitzHugh-Nagumo equation [12], the Brusselator [13], and the Gray-Scott model [14]. We obtained interconnected structures such as single-gyroid, double-gyroid, and diamond structures as well as lamellar, hexagonal-cylinder, body-centered-cubic sphere, and face-centered-cubic sphere structures.

In the present paper, we extend the previous studies and carry out numerical simulations of the Lengyel-Epstein model [15] which is a model system of the CIAM reaction. We consider inhomogeneous systems as well as ordinary homogeneous systems with periodic boundary conditions. There are two methods to realize an inhomogeneous system. One is to make a parameter in the time-evolution equations space-dependent and impose Dirichlet boundary conditions at the system boundaries assuming a constant supply of chemical reactants. The other is also to make a parameter space-dependent but with Neumann boundary conditions. Since a slightly modified chemical reaction, the chlorine dioxide-iodine-malonic acid (CDIMA) reaction, is photosensitive [16], such a space dependence with no flux condition is possible experimentally by illumination of light [17].

The Lengyel-Epstein model in one and two dimensions has been studied analytically and numerically. Jensen *et al.* have investigated the formation, growth, and pattern selection of Turing structures focusing on the effects of a strongly subcritical transition to stripes [18]. The model has also been analyzed under spatiotemporal forcing in one dimension [17] and under time-delayed global feedback in two dimensions [19].

Turing patterns in a homogeneous system in three dimensions have been investigated experimentally by Epstein and his coworkers [20]. They have observed by a tomographic technique, 3D stationary concentration patterns of the Belousov-Zhabotinsky reaction in microemulsions confined in a cylindrical capillary whose size is much larger than the characteristic length of patterns. This method is free from a concentration gradient caused by steady supply of chemical components from the system boundaries. However, regular interconnected patterns were not obtained in these experiments.

From a mathematical point of view, identification of what kinds of interconnected structures exist as a Turing pattern in three dimensions would be of interest since interconnected structures with cubic symmetry such as the gyroid are related, at least approximately, by periodic minimal surfaces [21]. This fact implies that Turing patterns in three dimensions might make a link between reaction-diffusion equations and geometry and topology of interfaces. It is also mentioned that Turing instability is mathematically related with microphase separation of block copolymers [22] and it has been established both experimentally and theoretically that interconnected structures such as the double gyroid exist as a micorphase separated state [23]. This fact is another motivation of our study in three dimensions.

Recently, systematic numerical simulations of the Lengyel-Rabai-Epstein model (from which the Lengyel-Epstein model is reduced) have been conducted in three dimensions under the boundary conditions corresponding to a gel strip reactor and have obtained domain patterns [24] which are qualitatively consistent with experiments [2]. In contrast to this study, our

main concern is interconnected structures. Our purpose of the present study is to confirm existence of interconnected Turing patterns in a homogeneous system of the Lengyel-Epstein model and to investigate how those patterns are modified in inhomogeneous situations.

The organization of the present paper is as follows. In Sec. II, we describe the Lengyel-Epstein model and numerical procedure for 3D reaction-diffusion systems. The Lengyel-Epstein model is solved numerically in Sec. III in homogeneous systems with periodic boundary conditions. We have found various interconnected periodic structures including the Schwartz P-surface structure. In Sec. IV, we investigate pattern formation where the concentrations have a spatial gradient under the Dirichlet boundary conditions. The case of Neumann boundary conditions is considered in Sec. V. The patterns obtained in Secs. IV and V are not precisely periodic because of the spatial gradience of the parameters. After eliminating this nonuniformity effect, we identify the patterns in Sec. VI. Discussion is given in Sec. VII.

II. THE LENGYEL-EPSTEIN MODEL

The Lengyel-Epstein (LE) model is given by the set of reaction-diffusion equations [15,17]

$$\frac{\partial u(\vec{r},t)}{\partial t} = \nabla^2 u(\vec{r},t) + a - cu(\vec{r},t) - \frac{4u(\vec{r},t)v(\vec{r},t)}{1+u(\vec{r},t)^2} - \phi, \tag{1}$$

$$\frac{1}{\sigma}\frac{\partial v(\vec{r},t)}{\partial t} = d\nabla^2 v(\vec{r},t) + cu(\vec{r},t) - \frac{u(\vec{r},t)v(\vec{r},t)}{1+u(\vec{r},t)^2} + \phi, \tag{2}$$

where a, c, σ, and d are positive constants. This is a simplified model of the CDIMA reaction. The variables $u(\vec{r},t)$ and $v(\vec{r},t)$ are dimensionless local concentrations of the activator and the inhibitor, respectively. The constant ϕ stands for the intensity of photoillumination.

The equilibrium uniform solution of Eqs. (1) and (2) is given by [17]

$$u_0 = \frac{a-5\phi}{5c}, \quad v_0 = \frac{a(1+u_0^2)}{5u_0}. \tag{3}$$

Substituting the deviations $\delta u(\vec{r},t) = u(\vec{r},t) - u_0$ and $\delta v(\vec{r},t) = v(\vec{r},t) - v_0$ into Eqs. (1) and (2) and linearizing them, we obtain the 2×2 linear matrix $\widetilde{L}_0$ whose i,j component is given by

$$\widetilde{l}_{11} = -\left(c + \frac{4(1-u_0^2)v_0}{(1+u_0^2)^2} + k^2\right), \quad \widetilde{l}_{12} = -\frac{4u_0}{1+u_0^2}, \tag{4}$$

$$\widetilde{l}_{21} = \sigma\left(c - \frac{(1-u_0^2)v_0}{(1+u_0^2)^2}\right), \quad \widetilde{l}_{22} = -\sigma\left(\frac{u_0}{1+u_0^2} + dk^2\right), \tag{5}$$

where $\vec{k}$ ($k = |\vec{k}|$) is the wave vector of the deviations, i.e., $\delta u, \delta v \sim \exp(i\vec{k}\cdot\vec{r})$. The eigenvalue of $\widetilde{L}_0$ is given by the solutions of the following equation:

$$\lambda^2 - (\widetilde{l}_{11} + \widetilde{l}_{22})\lambda + \mathrm{Det}\widetilde{L}_0 = 0. \tag{6}$$

The Turing instability occurs by the condition that

$$\mathrm{Det}\widetilde{L}_0 = \widetilde{l}_{11}\widetilde{l}_{22} - \widetilde{l}_{12}\widetilde{l}_{21} = 0. \tag{7}$$

The minimum of $\mathrm{Det}\widetilde{L}_0$ as a function of k is determined by $d\mathrm{Det}\widetilde{L}_0/dk^2 = 0$ as

$$-\widetilde{l}_{22} - \sigma\widetilde{l}_{11} = 0. \tag{8}$$

From Eqs. (7) and (8), we obtain the critical wave number k_c and the bifurcation threshold. For example, when $a = 16.0$, $c = 0.6$, $d = 1.07$, and $\sigma = 301.0$, the critical wave number is $k_c = 1.07$ and Turing patterns appear for $\phi < \phi_c \approx 2.3$ [17].

In order to investigate the time evolution in the region where the Turing instability occurs, we have carried out numerical simulations for the coupled set of Eqs. (1) and (2) in three dimensions. The space was divided into $N_x \times N_y \times N_z$ cubic cells with cell size δx. The simple Euler algorithm was used with time step δt which has to fulfill the stability condition caused by the diffusion terms. In each time step, we employ a 27-point difference scheme introduced in Ref. [25] to diminish the anisotropy caused by discretizing the Laplacian. The initial conditions are basically given by the equilibrium solutions (3) with small noises superimposed. We shall investigate the pattern evolution for periodic, Dirichlet, and Neumann boundary conditions in the subsequent sections.

To accelerate numerical computations, parallelization of source codes using graphics processing units (GPU) has recently been developed. We utilize the GPU with Compute Unified Device Architecture (CUDA) [26] to solve numerically the discretized equations of Eqs. (1) and (2). Molnar *et al.* [27] applied this method to several reaction-diffusion equations in three dimensions. Their main concern was not to explore Turing patterns but to check the efficiency of the numerical method.

III. PATTERNS UNDER PERIODIC BOUNDARY CONDITIONS

In this section, we present numerical results of Eqs. (1) and (2) in three dimensions where all the parameters are assumed to be constant. When $a = 16.0$, $c = 0.6$, $d = 0.683$, and $\sigma = 301.0$, Turing patterns are expected in the region $1.190 < \phi < 2.003$. Therefore, we have explored the patterns in this region for discrete values of $\phi = 1.15 + 0.05n$ with n positive integers.

The numerical procedure is the same as that in Ref. [11]. The system is divided into cubic cells with $N_x = N_y = N_z = 32$ and the periodic boundary conditions are imposed at the system boundaries. Since the spatial period of the stationary solutions is unknown before simulations, we change δx in the region $0.250 \leqslant \delta x \leqslant 0.550$ with the increment 0.002 to find the most stable periodic solution. The initial conditions are set to be $u = u_0$ and $v = v_0$ with small noises superimposed. In order to avoid freezing at any metastable states, we add white noises in the time-evolution equations at each time step with the intensity A. This intensity is also changed from 0 to 0.04 by the increment 0.005 to check the local stability of stationary solutions.

In this way, we have obtained 9 stationary patterns as listed in Fig. 1. The abbreviations L, H, DG, Fd, PL, B, P, SG, and SD indicate lamellar, hexagonal-cylinder, double-gyroid,

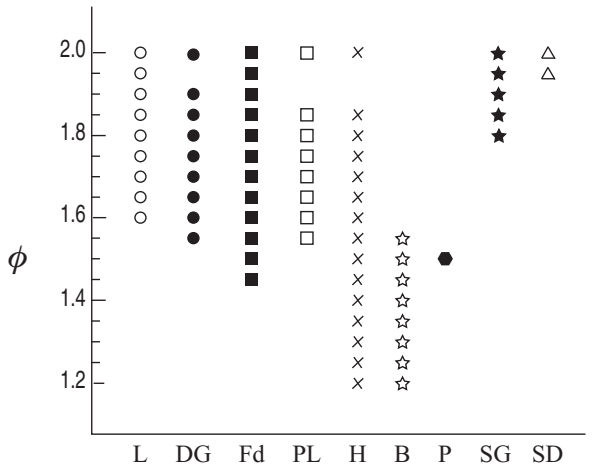

FIG. 1. Region of ϕ where 9 stationary solutions appear in the LE model. The meanings of L, DG, Fd, PL, H, B, P, SG, and SD are given in the text.

$Fddd$, perforated-lamellar, bcc, Schwartz P-surface, single-gyroid, and single-diamond structures, respectively. Note that there are several locally stable solutions for a given value of ϕ. For example, for $\phi = 1.6$ we have lamellar structure, double-gyroid, $Fddd$ structure, perforated-lamellar structure, and hexagonal structure of cylinders depending on δx, A, and the random initial conditions. The P-surface pattern was obtained only for $\phi = 1.50$. But this is reproducible. All the structures except for Schwartz P-surface were obtained in our pervious study [10,11] of the FitzHugh-Nagumo equation [12], the Brusselator [13], and the Gray-Scott model [14]. It is remarked here that no double-diamond structure was found either in the present study or in our previous study [11].

Domain evolution of the P-surface structure is shown in Fig. 2. Starting from a random initial condition in Fig. 2(a), domains grow and finally they constitute a periodic interconnected structure in Fig. 2(d). To identify this structure, we plot the Bragg positions in Fig. 2(e) and their intensity in Table I. The intensity is defined by

$$I_k = u_{\vec{k}} u_{-\vec{k}}, \tag{9}$$

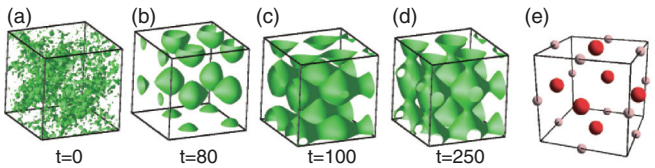

FIG. 2. (Color online) Formation of Schwartz P surface in Eqs. (1) and (2). (a)–(d) for $\phi = 1.50$, $N_x = N_y = N_z = 32$, $\delta x = 3.42 \times 10^{-1}$, $N = 32$, and $A = 0.005$ at (a) $t = 0$, (b) $t = 80$, (c) $t = 100$, and (d) $t = 250$. For the sake of clarity, the isosurface of $u = 2.848$ is represented in (a) whereas the isosurface of $u = 2.8$ is represented in (b)–(d). The Bragg spots for $I_k > 1.5 \times 10^{-4}$ obtained from the structure in (d) are shown in (e). The large 6 red spheres indicate the major Bragg positions and their mirror inversions whereas the small pink spheres indicate the secondary peak positions. These are listed in Table I below.

TABLE I. Bragg spots and their intensities (arbitrary units) of the Scwartz P-surface structure.

Peak position	I_k	Peak position	I_k
(2, 0, 0)	0.137 823	(2, 2, 0)	0.002 737
(0,2, 0)	0.137 816	(2, −2, 0)	0.002 734
(0, 0, 2)	0.137 788	(2, 0, −2)	0.002 737
(2, 0, 2)	0.002 735	(0, 2, 2)	0.002 737
(0, 2, −2)	0.002 735		

where $u_{\vec{k}}$ is given by

$$u_{\vec{k}} = \int d\vec{r} u(\vec{r}) \exp(i\vec{k} \cdot \vec{r}). \tag{10}$$

The Bragg positions defined by $\vec{k}_{Bragg} = \vec{k}L/(2\pi)$ in Table I are consistent with the isosurface representation of the Schwartz P surface [28]

$$0 = \cos x + \cos y + \cos z. \tag{11}$$

In fact, a domain structure similar to that in Fig. 2(d) can be obtained from Eq. (11).

It might be useful to compare the above results with those in two dimensions. We have carried out numerical simulations of Eqs. (1) and (2) with the same set of parameters under the periodic boundary conditions with $N_x = N_y = 256$ and $\delta x = 0.5$. Hexagonal-spot patterns appear for $1.95 \leqslant \phi \leqslant 2.0$ and $1.20 \leqslant \phi \leqslant 1.65$ and stripe patterns for $1.65 \leqslant \phi \leqslant 1.95$. This is qualitatively consistent with the regions of L and H in Fig. 1.

IV. CONCENTRATION GRADIENT UNDER DIRICHLET BOUNDARY CONDITION

When two continuous stirred tank reactors contact a reaction cell, the concentrations at the boundaries are fixed so that a concentration gradient of the chemical components is formed in the system [2]. In this section, we consider this case and assume that the parameter ϕ in Eqs. (1) and (2) depends on the space.

As in the preceding section, we set the parameters as $a = 16.0$, $c = 0.6$, $d = 0.683$, and $\sigma = 301.0$ so that the uniform state is linearly unstable in the region $1.190 < \phi < 2.003$. Throughout the present paper, we fix the parameters as above.

A. One-dimensional (1D) patterns with Dirichlet boundary condition

Before we discuss 3D patterns, we briefly describe formation of 1D patterns. In a system with size $L = N \times \delta x = 32$ ($N = 64$ and $\delta x = 0.5$), we impose

$$\phi(x) = \phi_{\min} + (\phi_{\max} - \phi_{\min})\frac{x}{L}, \tag{12}$$

where $\phi_{\max}$ and $\phi_{\min}$ are constants. The initial distributions of $u_0(x)$ and $v_0(x)$ are set as

$$u_0(x) = \frac{a - 5\phi(x)}{5c}, \tag{13}$$

$$v_0(x) = \frac{a[1 + u_0(x)^2]}{5u_0(x)}, \tag{14}$$

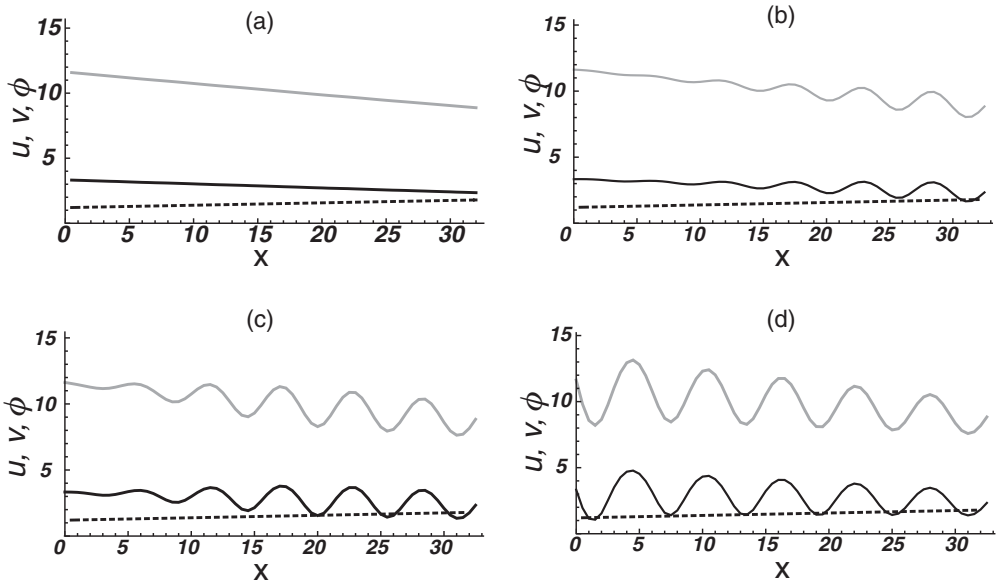

FIG. 3. Formation of spatial structure obtained from Eqs. (1), (2), and (12) for (a) $t = 0$, (b) $t = 60$, (c) $t = 86$, and (d) $t = 180$. The black line, the gray line, and the dotted line indicate u, v, and $\phi(x)$, respectively.

with small noises added. At each time step, white noises with amplitude A and no spatial correlations are added to Eqs. (1) and (2). The time evolution of domains is displayed in Fig. 3 for $\phi_{\min} = 1.20$, $\phi_{\max} = 1.80$, and $A = 0.005$. We find that a spatial structure starts to appear in the region of large $\phi(x)$ and propagates into the region of smaller $\phi(x)$ to form the final spatial structure.

It is interesting to see that the amplitude of the inhomogeneous structure is larger in the region of small ϕ although the domain evolution is slower there. Since the small ϕ region is close to the stability threshold $\phi = 1.19$, the slow dynamics is expected. The origin of the large amplitudes is probably related to the fact that the equilibrium values of u and v before the Turing instability occurs are larger near the $x = 0$ region.

B. 3D patterns with Dirichlet condition

In 3D simulations, we impose the Dirichlet condition at the boundaries $z = 0$ and $z = L_z$. At the boundaries perpendicular to the x axis and y axis, we impose the periodic boundary conditions.

To be specific, we set the z dependence of ϕ as

$$\phi(z) = \phi_{\min} + (\phi_{\max} - \phi_{\min})\frac{z}{L_z}, \tag{15}$$

where the parameters $\phi_{\min}$ and $\phi_{\max}$ are fixed shortly below. The space is divided as $(L_x, L_y, L_z) = (N_x \times \delta x, N_y \times \delta x, N_z \times \delta x)$ with $\delta x = 0.5$ and $(N_x, N_y, N_z) = (128, 128, 64)$ or $(128, 128, 128)$.

The values of u and v at the boundaries are given by

$$u(x,y,0,t) = \frac{a - 5\phi_{\min}}{5c}, \tag{16}$$

$$u(x,y,L_z,t) = \frac{a - 5\phi_{\max}}{5c}, \tag{17}$$

$$v(x,y,0,t) = \frac{a[1 + u(x,y,0,t)^2]}{5u(x,y,0,t)}, \tag{18}$$

$$v(x,y,L_z,t) = \frac{a[1 + u(x,y,L_z,t)^2]}{5u(x,y,L_z,t)}. \tag{19}$$

The initial conditions are put as

$$u_0^D(x,y,z,0) = \frac{a - 5\phi(z)}{5c}, \tag{20}$$

$$v_0^D(x,y,z,0) = \frac{a\left[1 + u_0^D(x,y,z,t)^2\right]}{5u_0^D(x,y,z,t)}, \tag{21}$$

where small noises are superimposed. Furthermore, to make the patterns relax to the final stationary state quickly, random noises are added to the time-evolution equations every time step, whose magnitude depends on z as

$$A(z) = A\frac{L_z - z}{L_z}. \tag{22}$$

Figure 4 displays the domain evolution (isosurface of $u = 2.0$) in the initial stage (a)–(d), in the late stage (e)–(g), and in the final stage (h) for $\phi_{\min} = 1.2$ and $\phi_{\max} = 1.8$, and the system size $(L_x, L_y, L_z) = (64, 64, 32)$ with $\delta x = 0.5$ and $A = 0.015$. Similarly to the one-dimensional case shown in Fig. 3, a periodic structure emerges first in the large $\phi(z)$ region [i.e., the bottom in (a)] and grows into the whole region perpendicularly to the z axis as can be seen in Figs. 4(a)–4(d). The stripe pattern oriented randomly is gradually ordered as in Figs. 4(e)–4(g) and eventually the final ordered structure is formed as in Fig. 4(h).

In order to identify the structure in Fig. 4(h) in detail, the patterns from three different directions are displayed in Fig. 5. It is clearly seen from Fig. 5(a) that flat domains are arrayed perpendicularly to the z axis near $z = 0$ and $z = L_z$. A close look indicates that the lowest two domains and the upper most

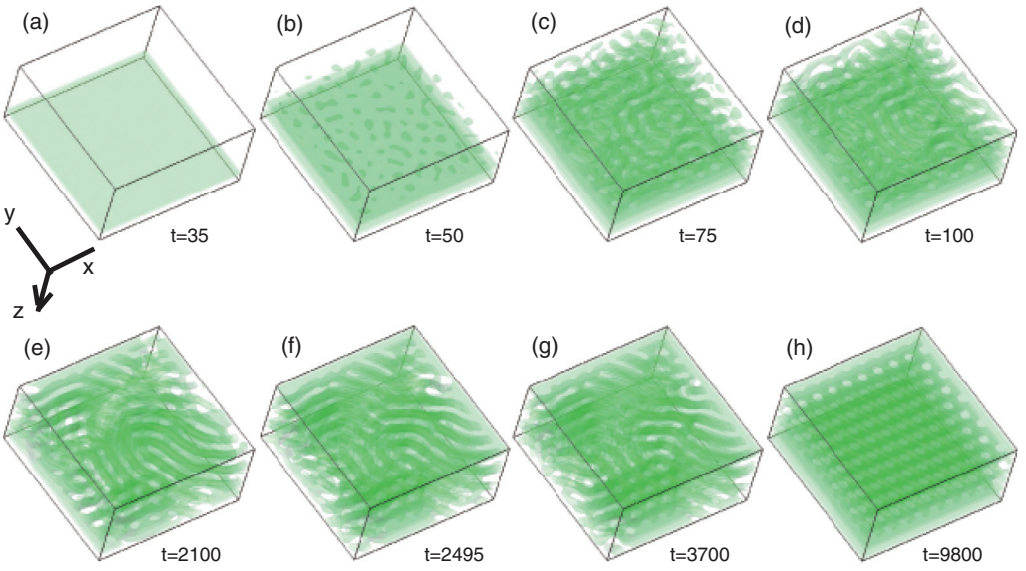

FIG. 4. (Color online) Formation of partially perforated-lamellar structure obtained from Eqs. (1) and (2) with (15)–(22) for $\phi_{\min} = 1.2$, $\phi_{\max} = 1.8$, and $A = 0.015$. Domains with the isosurface of $u = 2.0$ are represented. The Dirichlet condition is imposed at the z boundaries while the periodic conditions at the x and y boundaries. The illustration of optical transmittance of 50% has been used in this figure and figures below.

domain are board shaped while the middle three domains seem to be a perforated-lamellar structure. The holes in the domains are visible in Figs. 5(b) and 5(c). We note that the flat board-shaped domains close to the boundaries are not clearly seen there since the illustration of optical transmittance of 50% has been used.

The structure in the middle region of Fig. 5(a) is magnified in Fig. 6. The domain pattern in Fig. 6(a) is quite similar to that in Fig. 5(d) in Ref. [11], which is identified as a perforated-lamellar structure. It is evident from Fig. 6(b) that the location of holes constitutes a hexagonal pattern and they are stacked alternatively as $ABAB\ldots$ along the z axis. Furthermore, Figs. 6(a) and 6(b) indicate that the size of holes increases as z is increased. We will analyze this structure in further detail in Sec. VI eliminating the concentration gradients due to the boundary conditions.

It is remarked that the final structures depend on the initial conditions and random perturbations and that two other structures have been obtained for different runs. One is an ordered cylindrical structure sandwiched by flat board-shaped domains near the z boundaries. The other is a lamellar structure perpendicular to the z axis.

When we set a smaller gradient of ϕ such that $\phi_{\min} = 1.3$ and $\phi_{\max} = 1.4$ with $(L_x, L_y, L_z) = (64, 64, 32)$, $\delta x = 0.5$, and $A = 0.025$, we have a different domain evolution though not shown. That is, the final structure is an ordered cylindrical structure sandwiched by the flat board-shaped domains near the z boundaries as mentioned in the preceding paragraph. The cylindrical domains are arrayed perpendicularly to the z axis to form a hexagonal lattice. Formation of cylindrical domains is understood as follows. One notes that hexagonal cylindrical domain structure or bcc spherical domain structure is possible in the region $1.3 \leqslant \phi \leqslant 1.4$ in a homogeneous system as in Fig. 1. However, bcc structure is incompatible with the uniaxial symmetry caused by the gradient in the z direction and is unfavorable compared to the hexagonal structure. We have checked the same kind of cylindrical structures for other runs of simulations.

We have carried out numerical simulations for a wider system in the z direction as $(L_x, L_y, L_z) = (64, 64, 64)$. Other parameters are set to be $\phi_{\min} = 1.1$, $\phi_{\max} = 2.1$, $A = 0.035$,

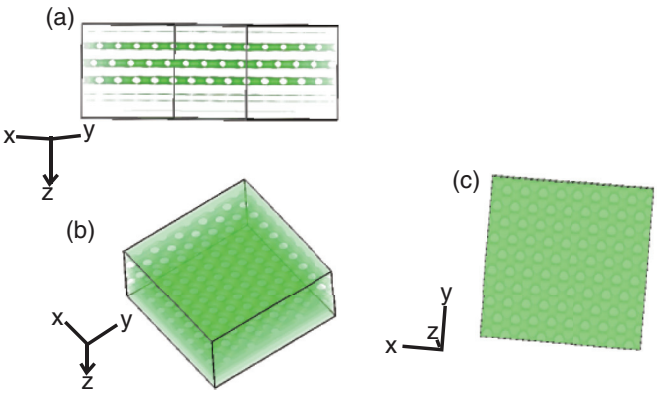

FIG. 5. (Color online) View of the final structure shown in Fig. 4(h) from three different directions.

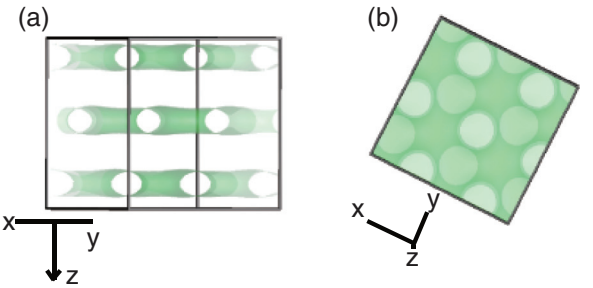

FIG. 6. (Color online) Magnification of the cubic region of $6 \leqslant z \leqslant 22$ in Fig. 4(h).

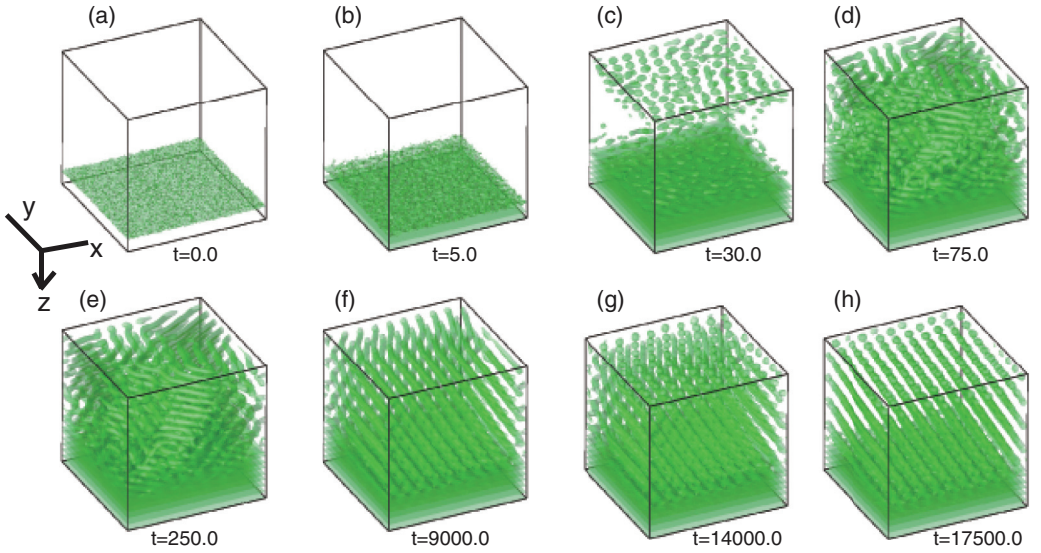

FIG. 7. (Color online) Mixture of lamellar, cylindrical, and spherical domains for $\phi_{\max} = 1.1$, $\phi_{\min} = 2.1$, $A = 0.035$, and $(L_x, L_y, L_z) = (64,64,64)$. The boundary conditions are the same as those in Fig. 4. Domain surface with the isosurfaces of $u = 2.0$ is displayed in the initial stage from (a) to (e) and in the late stage from (f) to (h).

and $\delta x = 0.5$. The gradient of ϕ along the z axis is equal to $1.0/64$, which is not much different from $0.6/32$ in Fig. 4. As mentioned above, the Turing instability occurs in the region $1.190 < \phi < 2.003$ and hence the system has a linearly stable region by the above choice of parameters. Figures 7(a)–7(e) show that domains appear initially in the region close to the z boundaries. As they grow, they gradually array in ordered configurations as Figs. 7(f)–7(h). Figure 8 displays the pattern in Fig. 7(h) viewed from two different directions. Spherical domains constitute a bcc structure. Spherical and cylindrical structures are formed in the small $\phi(z)$ region whereas a lamellar structure in the large $\phi(z)$ region. The order of these structures is transverse to the z direction.

Although not shown here, we have carried out numerical simulations for other sets of parameters $(\phi_{\min}, \phi_{\max}, A)$. In some cases, interconnected patterns are observed but only transiently. The structures obtained asymptotically in time are essentially the same as those presented above. Therefore, we conclude that interconnected periodic patters with cubic symmetry do not appear as a final structure in the gradient system with the Dirichlet boundary conditions.

Finally we make a remark that the domain evolution for a larger system as in Fig. 7 is qualitatively different from that in a smaller system as in Fig. 4. The final structure is reached quickly in Fig. 4 since the boundary condition has a strong influence in the whole system. On the other hand, there are two stages of domain growth in a large system. In an initial stage, domains grow randomly and then, in the second stage, those domains become ordered, which is a very slow process as can be seen in Fig. 7. This property can be seen in all the domain evolutions given below in three dimensions.

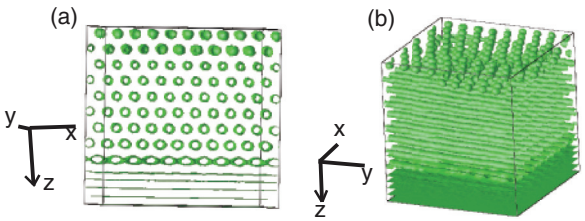

FIG. 8. (Color online) Structure of Fig. 7(h) viewed from two different directions.

V. CONCENTRATION GRADIENT UNDER NEUMANN BOUNDARY CONDITION

In this section, we consider a confined system with boundary walls and assume that chemical reactions are controlled by light illumination. The illumination is turned on at $t = 250$. That is, we set $\phi = 0$ for $0 < t < 250$ in Eqs. (1) and (2) whereas $\phi = \phi^{ON}(\vec{x}) \neq 0$ after $t = 250$. The system parameters are chosen such that the uniform state is stable for $\phi = 0$ but when $\phi = \phi^{ON}(\vec{x})$, a Turing instability occurs.

A. 1D patterns with Neumann condition

First, we examine pattern formation in one dimension under Neumann boundary conditions. We set $L = N \times \delta x = 64.0$ with $N = 128$ and $\delta x = 0.5$, and when $0 < t < 250$, $\phi = 0$. The initial condition is set as $u(x) = u_0$ and $v(x) = v_0$ which are the equilibrium values for $\phi = 0$. After $t = 250$ we put $\phi^{ON}(x)$ in Eqs. (1) and (2) as

$$\phi^{ON}(x) = \phi_{\min} + (\phi_{\max} - \phi_{\min})\frac{x}{L}, \tag{23}$$

where $\phi_{\min} = 1.1$ and $\phi_{\max} = 2.1$.

Figure 9 shows the domain evolution obtained by numerical calculations of Eqs. (1) and (2) adding random white noises of the amplitude $A = 0.01$ every time step and at the all space points. During the interval $0 < t < 250$, the values of u and v are almost equal to the equilibrium values as in Fig. 9(a). After $t = 250$, $\phi^{ON}(x)$ takes nonzero values as indicated by the black dotted line in Fig. 9(b) and then a periodic structure

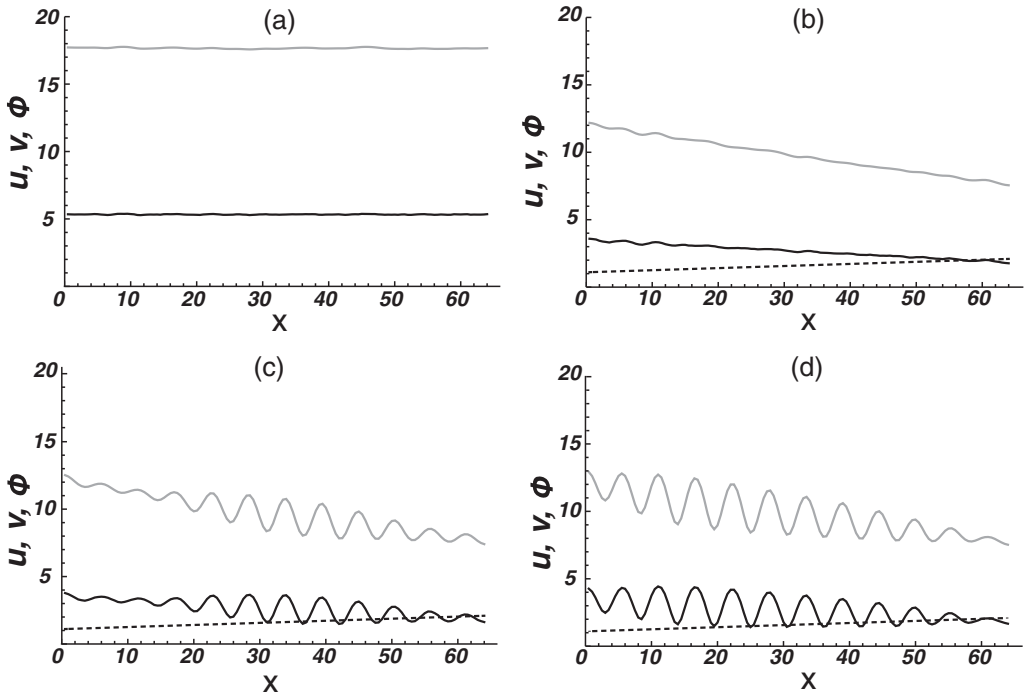

FIG. 9. Domain evolution in one dimension with Neumann boundary conditions for $\phi_{\min} = 1.1$ and $\phi_{\max} = 2.1$ in Eq. (23). The spatial profits of u (black line), v (gray line), and $\phi^{ON}(x)$ (dotted line) for (a) $t = 0.0$, (b) $t = 254$, (c) $t = 390$, and (d) $t = 550$.

starts to evolve in the whole region almost simultaneously as in Figs. 9(b) and 9(c) and finally the stationary structure as in Fig. 9(d) is formed. The growth rate of domains is large in the middle region. The uniform state is linearly stable for the values of $\phi^{ON}(x)$ in the regions $0 \leqslant x < 5.76$ and $57.792 < x \leqslant 64.0$. Note, however, that a periodic structure is induced even in the stable region although the amplitude is small there. If the noise is stronger as $A = 0.03$, the periodic structure is evolved more uniformly in both space and time.

B. 3D patterns with Neumann condition

In three dimensions, we apply the same time dependence of ϕ as in Sec. V A. After $t = 250$ we put $\phi^{ON}(z)$ as

$$\phi^{ON}(z) = \phi_{\min} + (\phi_{\max} - \phi_{\min})\frac{z}{L_z}. \tag{24}$$

The Neumann boundary conditions are imposed at the z boundaries whereas the periodic boundary conditions at the x and y boundaries. The initial conditions are given by the equilibrium solution (3). In order to accelerate the convergence

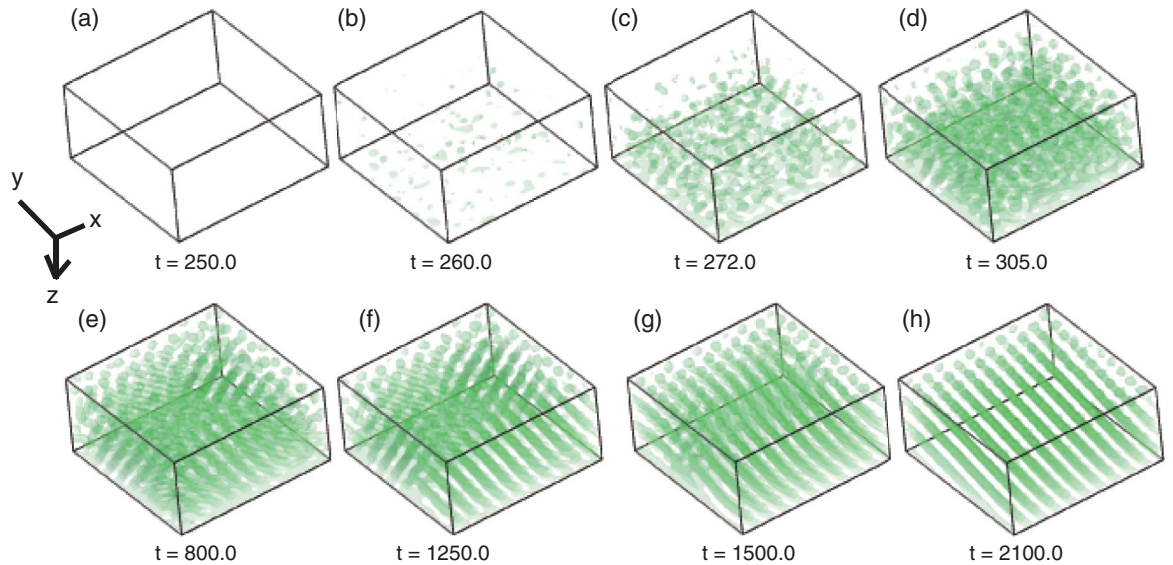

FIG. 10. (Color online) Cylindrical domain structure represented by the isosurface of $u = 2.0$ for $(L_x, L_y, L_z) = (64, 64, 32)$, $\delta x = 0.5$, $\phi_{\min} = 1.2$, $\phi_{\max} = 1.8$, and $A = 0.025$ under the Neumann boundary conditions at the z boundaries.

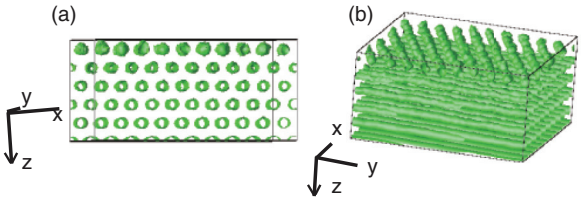

FIG. 11. (Color online) View of the pattern in Fig. 10(h) from two different directions.

of the numerical solutions for $t > 250$, we have added random white noises to u and v at every time step. The noise intensity A has a z dependence similarly to Eq. (22).

We have obtained the results shown in Fig. 10 for $(L_x,L_y,L_z) = (N_x \times \delta x, N_y \times \delta x, N_z \times \delta x) = (64,64,32)$ with $\delta x = 0.5$, $\phi_{\min} = 1.2$, $\phi_{\max} = 1.8$, and $A = 0.025$. No structure appears till $t = 250$ but after that, spherical and cylindrical domains are formed as in Figs. 10(b)–10(d) and ordered as in Figs. 10(e)–10(g). The final structure shown in Fig. 10(h) indicates that ordered spherical domains exist in the uppermost layer, below which an ordered cylindrical structure is constituted perpendicularly to the z axis. This can be seen more clearly in Fig. 11 viewed from different directions.

We obtain different structures when we set different initial distributions and random perturbations. One of them is an ordered cylindrical structure arrayed perpendicularly to the z axis to form a hexagonal lattice which occupies the whole volume. The other one is the lowest two domains which are board shaped while the upper three domains constitute a cylindrical structure arrayed perpendicularly to the z axis to form a hexagonal lattice.

Pattern formation for a wider system $(L_x,L_y,L_z) = (N_x \times \delta x, N_y \times \delta x, N_z \times \delta x) = (64,64,64)$ with $\delta x = 0.5$, and a wider range of ϕ as $\phi_{\min} = 1.1$, $\phi_{\max} = 2.1$, and $A = 0.02$ is displayed in Fig. 12. Some structures are formed in the region $1.10 \leqslant \phi(z) < 1.190$ and $2.003 < \phi(z) \leqslant 2.10$ although the uniform state is linearly stable in these regions. The three different views of the final structure in Fig. 12(h) are shown in Fig. 13. Figure 13(a) indicates that several layers from the top where $\phi(z)$ is small are occupied by the cylindrical domains arrayed perpendicularly to the z axis whereas the interconnected network structure and lamellae are seen in the lower region where $\phi(z)$ is large. Figure 14 is a magnified pattern in the cubic region of $36 \leqslant z \leqslant 52$, $48 \leqslant x \leqslant 64$, and $32 \leqslant y \leqslant 48$. The pattern in Fig. 14(b) is expected to be an $Fddd$ structure because it resembles the one shown in Fig. 4(d) in Ref. [11], which was identified as $Fddd$ structure. We will verify this in the next section by eliminating the concentration gradient. This is the same situation as in the narrower system of $L_x = L_y = 64$ and $L_z = 32$ mentioned above.

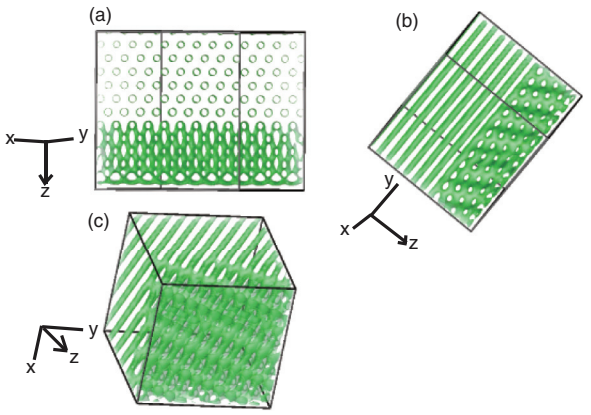

FIG. 13. (Color online) Three different views of the pattern in Fig. 12(h).

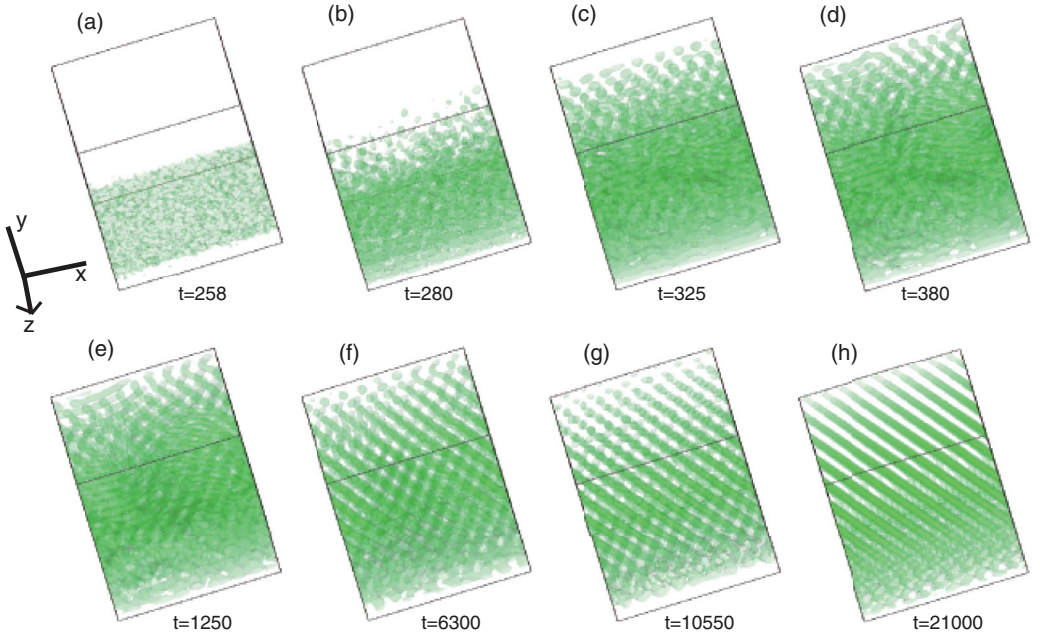

FIG. 12. (Color online) Mixed structure for $(L_x,L_y,L_z) = (64,64,64)$, $\delta x = 0.5$ with $\phi_{\min} = 1.1$, $\phi_{\max} = 2.1$, and $A = 0.02$ under the Neumann boundary condition at the z boundaries. Domain surface with the isosurfaces of $u = 2.0$ is displayed in the initial stage from (a) to (e) and in the late stage from (f) to (h).

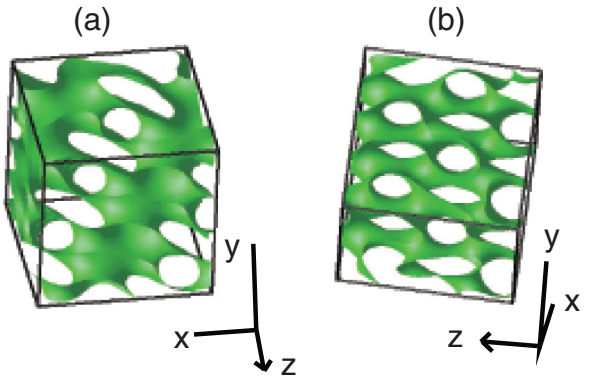

FIG. 14. (Color online) Magnification of the region $36.0 \leqslant z \leqslant 52.0$ in Fig. 12(h).

We obtain two other structures when we start with different initial distributions and random perturbations. One of them is an ordered cylindrical structure arrayed perpendicularly to the z axis to form a hexagonal lattice. The other is an inhomogeneous structure such that the lowest five domains are board shaped while the upper seven domains constitute a hexagonal structure of cylinders arrayed perpendicularly to the z axis.

When the gradient of ϕ is smaller as $\phi_{\min} = 1.6$ and $\phi_{\max} = 1.7$ with the system size $(L_x, L_y, L_z) = (64, 64, 32)$, $\delta x = 0.5$, and $A = 0.02$, an interconnected pattern appears in the whole system. However, this pattern does not attain a final time-independent state even at $t = 5 \times 10^5$ which is the longest simulation time in our study.

VI. PERIODIC INTERCONNECTED STRUCTURES

In this section, we investigate, in detail, the interconnected structures shown in Figs. 4(h) and 12(h). Since the system is inhomogeneous due to space dependence of the parameters in Eqs. (1) and (2), the concentration profiles of the Turing patterns are not strictly periodic in space. Therefore the simple Bragg point analysis in Sec. III is not applicable here. It is necessary to make the patterns periodic by eliminating the gradient effects before applying the Fourier analysis.

Construction of periodic structures

We describe the procedure to make the concentration profiles obtained in Secs. IV and V periodic in space.

(i) We subtract $\bar{u}_0(z)$ and $\bar{v}_0(z)$ from the concentration profiles u and v, respectively, where $\bar{u}_0(z)$ and $\bar{v}_0(z)$ are the profiles of u_0 and v_0 in Eq. (3) replacing ϕ by $\phi(z)$ defined by Eqs. (15) or (24). By choosing appropriately a constant value of ϕ^{try} which satisfies $\phi_{\min} \leqslant \phi^{\text{try}} \leqslant \phi_{\max}$, we add the steady uniform value of $u_0^{\text{try}} \equiv u_0(\phi^{\text{try}})$ and $v_0^{\text{try}} \equiv v_0(\phi^{\text{try}})$ to the concentration profiles.

(ii) We cut out the region of $M \times M \times M$ with M a positive integer in such a way that the cubic volume satisfies the periodic boundary conditions. Applying the expansion-contraction method of image processing, we transform the concentration pattern into another cubic system of $32 \times 32 \times 32$. The bilinear interoperation method is used for smoothing of the profiles between the lattice points.

(iii) The pattern obtained in this way is used as an initial condition to solve Eqs. (1) and (2) numerically in the cubic cell under the periodic boundary conditions. The size δx and the noise intensity A are chosen appropriately. In this way, we relax the pattern obtained in the process (ii).

If the profile is deformed substantially or destroyed in the process (iii), we change the set of the parameters ϕ^{try}, M, δx, and A and repeat the above steps. In what follows, we show two examples of patterns corrected by this procedure.

First, we apply the method to the interconnected structure shown in Fig. 4(h). We choose the area $45 \leqslant N_x \leqslant 72$, $56 \leqslant N_y \leqslant 83$, and $7 \leqslant N_z \leqslant 34$ with $M = 28$. Next we expand the cubic system slightly to another cubic volume with the size 32^3. We set $\phi^{\text{try}} = 1.35$, and make the interpolation of the concentration profiles. Figure 15(a) was obtained in this way. Then we apply the step (iii) with $\delta x = 0.52$ and $A = 0.0005$ to obtain Fig. 15(b) asymptotically in time. One can see that the domains in Fig. 15(b) are waving (though static) somehow compared to the domains in Fig. 15(a). Table II lists the Bragg spots and their intensities. From these analysis, we conclude that the structure in the central region of Fig. 4(h) is a perforated-lamellar structure [11].

TABLE II. Bragg spots and intensities for the perforated-lamellar structure of Fig. 15(b).

Peak position	I_k	Peak position	I_k
(0, 0, 3)	0.924 423	(2, 1, 2)	0.254 157
(2, −1, 2)	0.253 448	(0, 2, −2)	0.209 040
(2, 1, −1)	0.130 517	(2, −1, 1)	0.129 858
(0, 2, 1)	0.029 847		

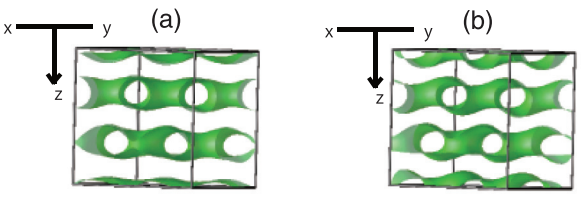

FIG. 15. (Color online) Interconnected structure of Fig. 4(h) after eliminating the concentration gradient (a) and the final relaxed structure (b). The isosurface with $u = 2.0$ is represented.

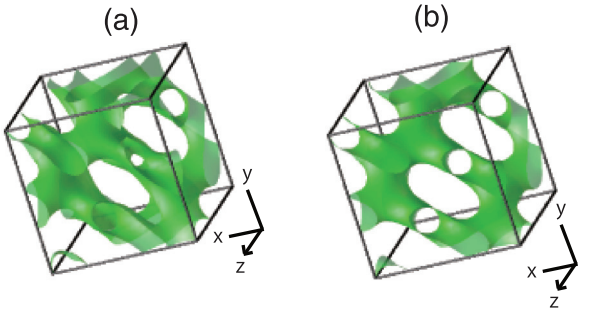

FIG. 16. (Color online) Interconnected structure of Fig. 13(h) after eliminating the concentration gradient (a) and the final relaxed structure (b). The isosurface with $u = 2.0$ is represented.

TABLE III. Bragg spots and intensities for the $Fddd$ structure of Fig. 16(b).

Peak position	I_k	Peak position	I_k
(2, 1, 1)	0.124 307	(2, −1, −1)	0.124 285
(1, 2, −1)	0.123 848	(1, 2, 1)	0.123 733
(2, −2, 0)	0.015 368	(1, −1, 2)	0.005 912
(1, −1, −2)	0.005 644	(1, 1, 1)	0.001 554
(0, 3, −1)	0.001 201	(0, 3, 1)	0.001 107
(3, 0, −1)	0.001 102	(3, 0, −1)	0.001 084

Next, we apply the method to Fig. 12(h). The volume with $M = 33$, such that $95 \leqslant N_x \leqslant 127$, $63 \leqslant N_y \leqslant 95$, and $85 \leqslant N_z \leqslant 117$, is chosen and then the size is shortened slightly to 32^3 with $\phi^{\text{try}} = 1.8$. The profile after interpolation is shown in Fig. 16(a). This pattern is relaxed with the parameters $\delta x = 0.460$ and $A = 0.0015$ to obtain Fig. 16(b). One notes that some distortions in Fig. 16(a) have disappeared in Fig. 16(b). From the data of the Brag peaks in Table III, we identify this structure with an $Fddd$ structure [11].

VII. DISCUSSION

We have shown the results of numerical simulations of the Lengyel-Epstein model in three dimensions. In a homogeneous system with periodic boundary conditions we have obtained interconnected periodic structures: single-gyroid, double-gyroid, single-diamond, Schwartz P-surface, perforated-lamellar, and $Fddd$ structures as well as lamellar, hexagonal-cylinder, and body-centered-cubic structures. All the structures except for the Schwartz P-surface structure were obtained in our previous study of three different reaction-diffusion systems [11]. We emphasize that although the Schwartz P-surface structure appears in a very narrow parameter region, this is reproducible by numerical simulations.

We have investigated how the patterns are modified when inhomogeneity due to boundary conditions is taken into account. We have considered two cases. One is the system where Dirichlet boundary conditions are imposed in the z boundaries whereas periodic boundary conditions are in the x and y boundaries. The other system has Neumann boundary conditions for the z boundaries and periodic boundary conditions for the x and y boundaries. We have found perforated-lamellar structure and $Fddd$ structure as interconnected patterns after correcting the gradient effects. These results are quite reasonable since both structures have a uniaxial symmetry which is consistent with the symmetry of the system with inhomogeneity along one spatial direction.

Therefore, we have confirmed in the present study as well as the previous ones [11] that interconnected periodic structures exist generically as Turing patterns in three dimensions. In particular, since the Lengyel-Epstein model is closely related with the realistic chemical reactions, it is our desire that the predictions given here will be observed experimentally in the near future.

From the theoretical point of view, there are many unexplored problems in three-dimensional Turing patterns. One needs to develop nonlinear reduction theories to study the structures and the dynamics as analytically as possible. See, for example, [29]. Amplitude equations might be derived for lamellar and cylindrical domain structures. However, it seems difficult to apply this method to interconnected structures since much more fundamental modes are involved. A phase-dynamical approach would be suitable for general periodic interconnected structures as would the elastic theory for double-gyroid and diamond structures in microphase separation [30]. Investigation of internal structures and stability of a boundary between different interconnected structures is also a challenging future problem in Turing patterns.

ACKNOWLEDGMENTS

This work was supported by a Grant-in-Aid for Scientific Research (A) (No. 24244063) and a Grant-in-Aid for Young Scientists (B) (No. 26800225) from MEXT of Japan.

[1] A. M. Turing, Phil. Trans. R. Soc. London, Ser. B **237**, 37 (1952).
[2] V. Castets, E. Dulos, J. Boissonade, and P. De Kepper, Phys. Rev. Lett. **64**, 2953 (1990).
[3] J. J. Perraud, K. Agladze, E. Dulos, and P. De Kepper, Physica A **188**, 1 (1992).
[4] Q. Ouyang and H. L. Swinney, Nature (London) **352**, 610 (1991).
[5] Q. Ouyang, Z. Noszticzius, and H. L. Swinney, J. Phys. Chem. **96**, 6773 (1992).
[6] D. Walgraef, *Spatio-Temporal Pattern Formation* (Springer, New York, 1996).
[7] A. De Wit, G. Dewel, P. Borckmans, and D. Walgraef, Physica D **61**, 289 (1992).
[8] A. De Wit, P. Borckmans, and G. Dewel, Proc. Natl. Acad. Sci. USA **94**, 12765 (1997).
[9] T. Leppanen, M. Karttunen, K. Kaski, R. A. Barrio, and L. Zhang, Physica D **168**, 35 (2002).
[10] H. Shoji, K. Yamada, and T. Ohta, Phys. Rev. E **72**, 065202(R) (2005).
[11] H. Shoji, K. Yamada, D. Ueyama, and T. Ohta, Phys. Rev. E **75**, 046212 (2007).
[12] R. FitzHugh, Biophys. J. **1**, 445 (1961); J. Nagumo, S. Arimoto, and S. Yoshizawa, Proc. IRE **50**, 2061 (1962).
[13] I. Prigogine and R. Lefever, J. Chem. Phys. **48**, 1695 (1968).
[14] P. Gray and S. K. Scott, Chem. Eng. Sci. **38**, 29 (1983).
[15] I. Lengyel and I. R. Epstein, Science **251**, 650 (1991).
[16] A. K. Horvath, M. Dolnik, A. M. Ahabotinsky, and I. R. Epstein, J. Phys. Chem. A **104**, 5766 (2000).
[17] S. Rüdiger, D. G. Míguez, A. P. Muñuzuri, F. Sagués, and J. Casademunt, Phys. Rev. Lett. **90**, 128301 (2003).
[18] O. Jensen, V. O. Pannbacker, E. Mosekilde, G. Dewel, and P. Borckmans, Phys. Rev. E **50**, 736 (1994).
[19] P. Ghosh, Phys. Rev. E **84**, 016222 (2011).
[20] T. Bansagi Jr., V. K. Vanag, and I. R. Epstein, Science **331**, 1309 (2011).
[21] S. T. Hyde and F. E. Schroeder-Turk, Interface Focus **2**, 529 (2012).

[22] T. Ohta, A. Ito, and A. Tetsuka, Phys. Rev. A **42**, 3225 (1990).
[23] T. Ohta, in *Kinetics of Phase Transitions*, edited by S. Puri and V. Wadhawan (CRC Press, New York, 2009).
[24] P. K. Moore and W. Horsthemke, Chaos **19**, 043116 (2009).
[25] A. Shinozaki and Y. Oono, Phys. Rev. E **48**, 2622 (1993).
[26] NVIDIA Corporation, NVIDIA CUDA Programming Guide, http://docs.nvidia.com/cuda/pdf/CUDA_C_Programming_Guide.pdf.
[27] F. Molnar Jr., F. Izak, R. Meszaros, and I. Lagzi, Chemom. Intell. Lab. Syst. **108**, 76 (2011).
[28] A. Aksismentiev, M. Fialkowski, and R. Holyst, Adv. Chem. Phys. **121**, 141 (2002).
[29] R. C. Desai and R. Kapral, *Dynamics of Self-Organized and Self-Assembled Structures* (Cambridge University Press, New York, 2009).
[30] K. Yamada and T. Ohta, Europhys. Lett. **73**, 614 (2006).